Crystallization and preliminary X-ray analysis of monalysin, a novel β-pore-forming toxin from the entomopathogen *Pseudomonas entomophila*

Maryline Blemont,[a] Renaud Vincentelli,[a] Christine Kellenberger,[a] Onya Opota,[b] Bruno Lemaitre,[c] Alain Roussel[a] and Philippe Leone[a]*

[a]Architecture et Fonction des Macromolécules Biologiques (AFMB), UMR 7257 CNRS et Aix–Marseille Université, Marseille, France, [b]Institute of Microbiology, University of Lausanne and University Hospital Centre, Lausanne, Switzerland, and [c]Global Health Institute, Ecole Polytechnique Fédérale Lausanne (EPFL), Lausanne, Switzerland

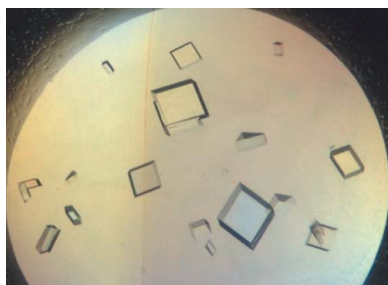Correspondence e-mail:
philippe.leone@afmb.univ-mrs.fr

Monalysin was recently described as a novel pore-forming toxin (PFT) secreted by the *Drosophila* pathogen *Pseudomonas entomophila*. Recombinant monalysin is multimeric in solution, whereas PFTs are supposed to be monomeric until target membrane association. Monalysin crystals were obtained by the hanging-drop vapour-diffusion method using PEG 8000 as precipitant. Preliminary X-ray diffraction analysis revealed that monalysin crystals belonged to the monoclinic space group $C2$, with unit-cell parameters $a = 162.4$, $b = 146.2$, $c = 144.4$ Å, $\beta = 122.8°$, and diffracted to 2.85 Å resolution using synchrotron radiation. Patterson self-rotation analysis and Matthews coefficient calculation indicate that the asymmetric unit contains nine copies of monalysin. Heavy-atom derivative data were collected and a Ta_6Br_{14} cluster derivative data set confirmed the presence of ninefold noncrystallographic symmetry.

1. Introduction

Pore-forming toxins (PFTs) represent the largest class of bacterial protein toxins and are often important virulence factors of a pathogen (Iacovache *et al.*, 2010). These proteins are initially produced as soluble molecules. Association with a target membrane, generally *via* specific receptors, induces their oligomerization in a ring-like structure. Subsequent structural rearrangements of each protomer generate an amphipathic surface large enough to drive spontaneous membrane insertion, leading to the formation of a water-filled pore. Depending on the PFT, pore formation is aimed at permeabilizing the target membrane or can serve as a translocation channel to introduce other virulence factors into the target cell.

PFTs can be divided into two major classes according to the secondary structure of the membrane-spanning region: β-barrel (β-PFT) and α-helical (α-PFT). Monalysin was recently identified as a new virulence factor secreted by the *Drosophila* pathogen *Pseudomonas entomophila* (Opota *et al.*, 2011). Genetic studies suggested that this protein is involved in the ability of the pathogen to induce intestinal cell damage in the host gut. We previously produced recombinant monalysin from *Escherichia coli* culture and the various studies that we carried out (sequence alignment, circular dichroism, cytotoxicity assays and planar lipid bilayer experiments) indicated that monalysin is a β-PFT. Furthermore, multi-angle light-scattering analysis and electron-microscopy studies suggested that in solution monalysin is a multimeric protein with a ring-like conformation. This is in contradiction with what has been observed for all other PFTs studied until now. Indeed, the oligomerization of PFTs and subsequent organization in a ring-like structure are supposed to be induced by association with the target membrane. The structures of several PFTs have been determined, but the structures of both the soluble and the pore forms are available for only a few: the α-PFT ClyA (Wallace *et al.*, 2000; Mueller *et al.*, 2009) and the β-PFTs cytolysin (Olson & Gouaux, 2005; De & Olson, 2011) and γ-haemolysin (Olson *et al.*, 1999; Roblin *et al.*, 2008; Yamashita *et al.*, 2011). Nevertheless, the molecular mechanisms involved in the soluble-to-transmembrane-form transition of PFTs are still unknown.

Here, we present the crystallization and preliminary X-ray analysis of recombinant monalysin.

2. Experimental procedures

2.1. Protein expression and purification

The cloning and production of monalysin were performed as described previously (Opota *et al.*, 2011). Briefly, monalysin (residues 1–271) was cloned into pETG-20A vector to generate a construct encoding monalysin with an N-terminal fusion composed of the thioredoxin (TRX) protein followed by a 6×His tag and a *Tobacco etch virus* (TEV) protease cleavage site. TEV cleavage is used to liberate the fusion, leaving an extra serine residue at the monalysin N-terminus. Monalysin was expressed in Rosetta (DE3) pLysS *E. coli* cells (Novagen). After cell lysis, the protein was purified from the soluble fraction by nickel-affinity chromatography and was desalted to eliminate imidazole. After an overnight incubation at 277 K with 1:20(*w*:*w*) 6×His-TEV protease, monalysin was collected from the flowthrough of a second nickel purification and further purified by size-exclusion chromatography in 10 mM Tris pH 8, 500 mM NaCl. For crystallization trials, the purified monalysin was concentrated to 6.5 mg ml^{-1} by centrifugation using an Amicon 30 kDa cutoff concentrator in the same buffer as was used for size-exclusion chromatography. The protein concentration was determined from the absorbance at 280 nm using a NanoDrop 2000 (Thermo Scientific).

2.2. Crystallization and data collection

Initial crystallization trials were performed by the sitting-drop vapour-diffusion method at 293 K in 96-well Greiner plates with the Wizard I and II (Emerald BioSystems), PEGs Suite (Qiagen) and Crystal Screen and Crystal Screen 2 (Hampton Research) screens using a Cartesian HoneyBee robot (Genomic Solutions). Drops were prepared by mixing different volumes (100, 200 and 300 nl) of protein solution and 100 nl precipitant solution and were equilibrated against a 150 µl reservoir volume. Crystallization hits occurred in several conditions, especially Wizard I condition No. 7 [0.1 M MES pH 6.0, 0.2 M zinc acetate, 10%(*w*/*v*) PEG 8000]. After optimization, the final crystallization conditions were 0.1 M sodium acetate pH 4.6, 0.13 M zinc acetate, 0.6–1.1 M ammonium acetate, 2–7%(*w*/*v*) PEG 8000, with a protein:precipitant ratio of 3:1(*v*:*v*) in 1.5 µl hanging drops. Crystals appeared within a few days and were briefly soaked in crystallization solution supplemented with 20%(*v*/*v*) glycerol before being flash-cooled in a nitrogen-gas stream at 100 K. Native monalysin X-ray diffraction data (180 images with 1° Δφ, 5 s exposure and
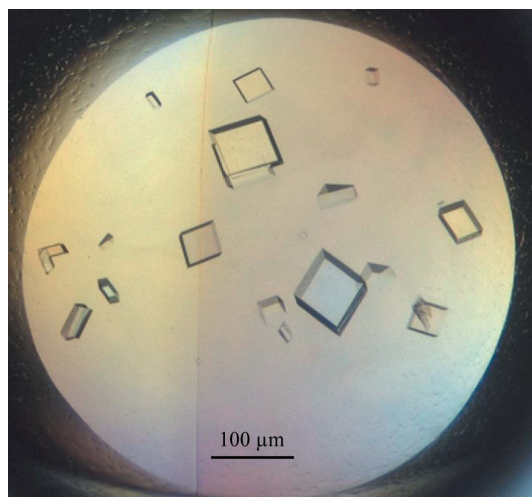

Figure 1
Crystals of native monalysin.

Table 1
Data-collection statistics for monalysin.

Values in parentheses are for the outermost resolution shell.

	Native	Ta$_6$Br$_{14}$ cluster derivative
Wavelength (Å)	0.87260	1.25452
Space group	$C2$	$C2$
Unit-cell parameters (Å, °)	$a = 162.4$, $b = 146.2$, $c = 144.4$, $\beta = 122.8$	$a = 160.7$, $b = 146.4$, $c = 147.0$, $\beta = 118.3$
Resolution (Å)	30–2.85 (3.00–2.85)	30–3.60 (3.79–3.60)
Unique reflections	65957 (9623)	34322 (4951)
Multiplicity	3.4 (3.4)	6.2 (6.3)
Completeness (%)	99.8 (99.9)	98.8 (98.6)
$\langle I/\sigma(I)\rangle$	13.0 (2.1)	11.9 (2.2)
R_{meas}† (%)	11.3 (77.5)	16.5 (97.6)
$R_{p.i.m.}$‡ (%)	6.0 (40.9)	6.5 (38.3)
Mosaicity (°)	0.22	0.24

† $R_{meas} = \sum_{hkl}\{N(hkl)/[N(hkl)-1]\}^{1/2}\sum_i |I_i(hkl) - \langle I(hkl)\rangle|/\sum_{hkl}\sum_i I_i(hkl)$, where $I_i(hkl)$ is the observed intensity and $\langle I(hkl)\rangle$ is the average intensity from $N(hkl)$ observations (symmetry-related and duplicate measurements of a unique reflection). ‡ $R_{p.i.m.} = \sum_{hkl}\{1/[N(hkl)-1]\}^{1/2}\sum_i |I_i(hkl) - \langle I(hkl)\rangle|/\sum_{hkl}\sum_i I_i(hkl)$.

Table 2
Phasing statistics of Ta$_6$Br$_{14}$ cluster derivative monalysin.

	Initial three Ta$_6$Br$_{14}$ clusters	Deduced nine Ta$_6$Br$_{14}$ clusters
CC (all/weak)†	30.24/12.99	
Phasing power‡	7.90	8.59
R_{cullis}§	0.26	0.25
FOM (centric/acentric)¶	0.571/0.178	0.581/0.212
Cluster occupancies	0.57/0.63/0.86	0.59/0.80/0.39/0.41/0.32/0.22/0.22/0.33/0.18

† The correlation coefficient as defined in the program *SHELXD* used within *autoSHARP*. ‡ The phasing power as defined in *SHARP*. § R_{cullis} as defined in *SHARP*. ¶ Figure of merit as defined in *SHARP*, calculated with centric or acentric reflections.

a crystal-to-detector distance of 306.42 mm) were collected to 2.85 Å resolution on beamline ID23-2 at the European Synchrotron Research Facility (ESRF), Grenoble, France using a MAR225 detector.

A heavy-atom derivative search was carried out by soaking crystals for different times in a solution containing 1–50 mM of various heavy atoms. Successful derivatization was achieved by soaking native monalysin crystals in 1 mM hexatantalum tetradecabromide (Ta$_6$Br$_{14}$ cluster; Knäblein *et al.*, 1997) for 2–5 d. The crystals were back-soaked for a few minutes in crystallization solution supplemented with 20%(*v*/*v*) glycerol before being flash-cooled in a nitrogen-gas stream at 100 K. Ta$_6$Br$_{14}$ cluster derivative X-ray diffraction data (480 images with 0.75° Δφ, 1 s exposure and a crystal-to-detector distance of 345.14 mm) were collected to 3.6 Å resolution at the tantalum peak wavelength on beamline ID23-1 at the ESRF using an ADSC Quantum Q315r detector.

2.3. X-ray crystallographic analysis

The data sets were integrated with *XDS* (Kabsch, 2010) and scaled with *SCALA* (Evans, 2006) from the *CCP*4 suite v.6.3.0 (Winn *et al.*, 2011). Data-collection statistics are reported in Table 1. Patterson self-rotation calculation was performed with *MOLREP* (Vagin & Teplyakov, 2010). Matthews coefficients and electron-density maps were calculated with the programs *MATTHEWS_COEF* and *FFT* from the *CCP*4 suite v.6.3.0, respectively. Heavy-atom substructure determination, positional refinement and phase calculations were performed using the programs *autoSHARP* (Vonrhein *et al.*, 2007) and *SHARP* (Bricogne *et al.*, 2003). Phasing statistics are reported in Table 2.

3. Results and discussion

Biophysical, functional and preliminary electron-microscopy studies of monalysin have been carried out previously (Opota *et al.*, 2011). In order to further characterize this novel PFT, we decided to solve its atomic structure by X-ray crystallography. After crystallization optimization, we obtained reproducible crystals (Fig. 1) that grew in a few days. Owing to anisotropic diffraction, about 100 crystals were tested and the best diffracted to 2.85 Å resolution. The Patterson self-rotation map shows the presence of ninefold noncrystallographic symmetry (NCS). The Matthews coefficient calculated with nine molecules is 2.64 $\text{Å}^3 \text{Da}^{-1}$ (which corresponds to an estimated solvent content of 53.5%), indicating that nine monalysin monomers

are present in the asymmetric unit (Matthews, 1968; Fig. 2). However, a previous multi-angle light-scattering analysis revealed that monalysin is composed of 18 monomers in solution. Therefore, it is highly likely that the content of the asymmetric unit is one half of the monalysin oligomer.

Monalysin presents no sequence homology to any protein of known structure. Therefore, it was necessary to solve the phase problem by means of multiple isomorphous replacement or multiple-wavelength anomalous dispersion methods. In a first attempt, seleno-methionine-substituted monalysin crystals were obtained and a data set was collected only at the selenium peak wavelength owing to radiation damage. However, no selenium site could be identified. In another approach, more than 60 native monalysin crystals were
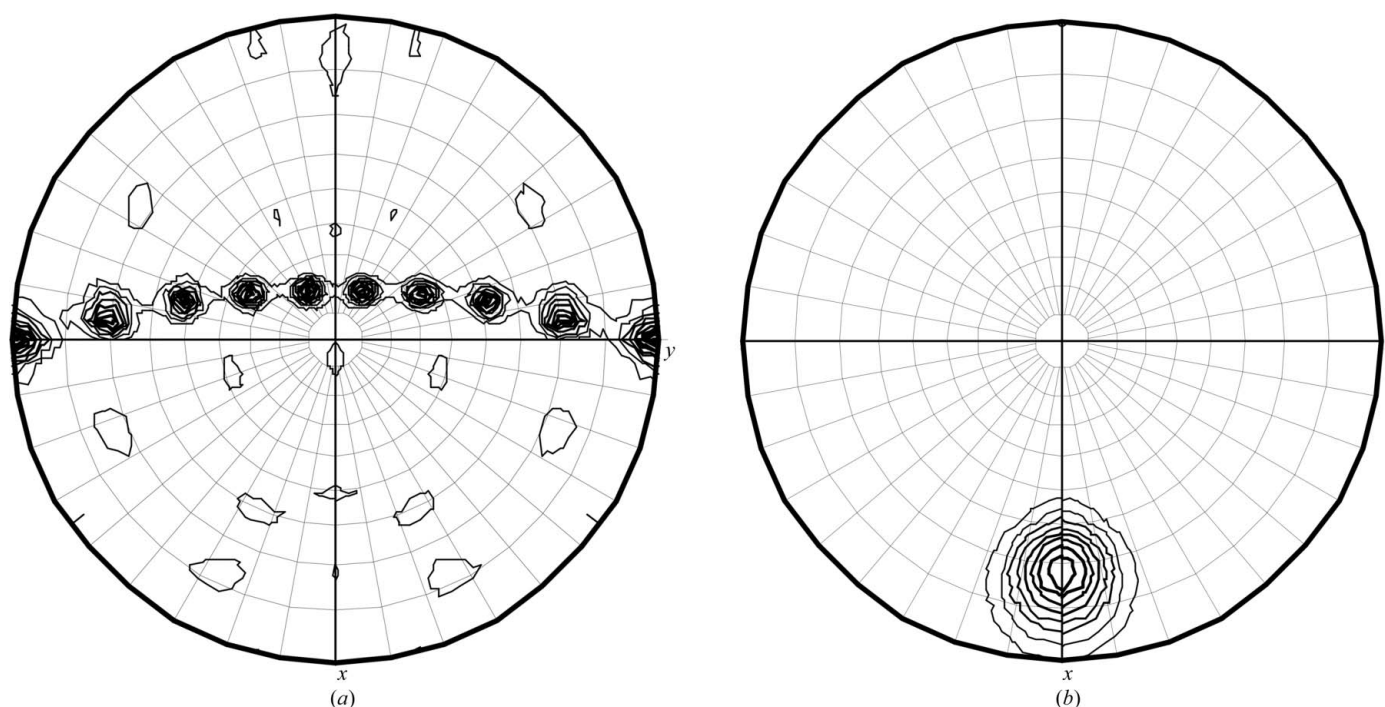

Figure 2
Stereographic projection of the Patterson self-rotation function calculated with the native monalysin data set in the range 20–5 Å and with a radius of integration of 30 Å. (*a*) Section with $\kappa = 180°$ displaying the nine twofold NCS axes. (*b*) Section with $\kappa = 40°$ displaying the ninefold NCS axis.

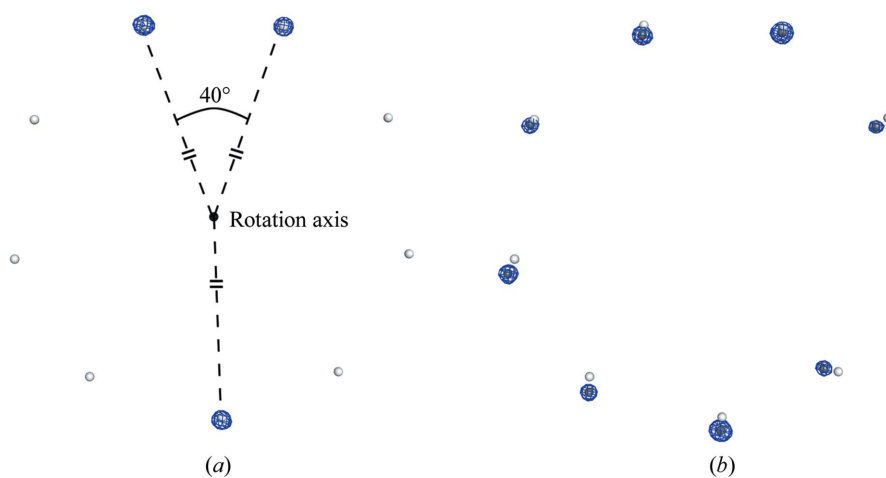**Figure 3**
The anomalous difference Fourier map calculated with the Ta_6Br_{14} cluster derivative data set (in blue and contoured at 6σ) reveals ninefold NCS of the cluster substructure in the asymmetric unit. (*a*) The initial substructure of three Ta_6Br_{14} clusters determined with the programs *autoSHARP* and *SHARP* was used to locate the rotation axis (black sphere) and to deduce the position of the six remaining clusters (light grey spheres). (*b*) Positional refinement and phase calculation performed with *SHARP* confirmed the ninefold NCS of the Ta_6Br_{14} clusters (dark spheres).

soaked in various heavy-atom derivatives and were tested on beamlines ID29 and ID23 at the ESRF and on the PROXIMA1 beamline at the SOLEIL synchrotron. Of the 22 data sets collected (only at the heavy-atom peak wavelength owing to radiation damage), the Ta_6Br_{14} cluster derivative data set gave satisfying results and was used to obtain phases using the single-wavelength anomalous dispersion (SAD) method.

An initial substructure of three Ta_6Br_{14} clusters was determined by *autoSHARP* and *SHARP*. On the basis of the Patterson self-rotation analysis, we speculated that the asymmetric unit might contain a heavy-atom substructure with ninefold NCS (Fig. 2). Thus, the positions of the three Ta_6Br_{14} clusters were used to approximately locate the ninefold axis, and the positions of the six putative remaining clusters were deduced by applying a $40°$ rotation around this axis using the program *TURBO-FRODO* (Roussel & Cambillau, 1991). Positional refinement of the nine Ta_6Br_{14} clusters and phase calculation were then performed with *SHARP*. Analysis of the resulting anomalous difference Fourier map confirmed the ninefold NCS of the Ta_6Br_{14} cluster substructure in the asymmetric unit (Fig. 3). The next step will be to improve the phases through solvent flattening, histogram matching and NCS averaging.

References

Bricogne, G., Vonrhein, C., Flensburg, C., Schiltz, M. & Paciorek, W. (2003). *Acta Cryst.* D**59**, 2023–2030.

De, S. & Olson, R. (2011). *Proc. Natl Acad. Sci. USA*, **108**, 7385–7390.

Evans, P. (2006). *Acta Cryst.* D**62**, 72–82.

Iacovache, I., Bischofberger, M. & van der Goot, F. G. (2010). *Curr. Opin. Struct. Biol.* **20**, 241–246.

Kabsch, W. (2010). *Acta Cryst.* D**66**, 133–144.

Knäblein, J., Neuefeind, T., Schneider, F., Bergner, A., Messerschmidt, A., Löwe, J., Steipe, B. & Huber, R. (1997). *J. Mol. Biol.* **270**, 1–7.

Matthews, B. W. (1968). *J. Mol. Biol.* **33**, 491–497.

Mueller, M., Grauschopf, U., Maier, T., Glockshuber, R. & Ban, N. (2009). *Nature (London)*, **459**, 726–730.

Olson, R. & Gouaux, E. (2005). *J. Mol. Biol.* **350**, 997–1016.

Olson, R., Nariya, H., Yokota, K., Kamio, Y. & Gouaux, E. (1999). *Nature Struct. Biol.* **6**, 134–140.

Opota, O., Vallet-Gély, I., Vincentelli, R., Kellenberger, C., Iacovache, I., Gonzalez, M. R., Roussel, A., van der Goot, F. G. & Lemaitre, B. (2011). *PLoS Pathog.* **7**, e1002259.

Roblin, P., Guillet, V., Joubert, O., Keller, D., Erard, M., Maveyraud, L., Prévost, G. & Mourey, L. (2008). *Proteins*, **71**, 485–496.

Roussel, A. & Cambillau, C. (1991). *Silicon Graphics Geometry Partners Directory*, p. 86. Mountain View: Silicon Graphics.

Vagin, A. & Teplyakov, A. (2010). *Acta Cryst.* D**66**, 22–25.

Vonrhein, C., Blanc, E., Roversi, P. & Bricogne, G. (2007). *Methods Mol. Biol.* **364**, 215–230.

Wallace, A. J., Stillman, T. J., Atkins, A., Jamieson, S. J., Bullough, P. A., Green, J. & Artymiuk, P. J. (2000). *Cell*, **100**, 265–276.

Winn, M. D. *et al.* (2011). *Acta Cryst.* D**67**, 235–242.

Yamashita, K., Kawai, Y., Tanaka, Y., Hirano, N., Kaneko, J., Tomita, N., Ohta, M., Kamio, Y., Yao, M. & Tanaka, I. (2011). *Proc. Natl Acad. Sci. USA*, **108**, 17314–17319.